Implications of parasitic absorption of Electron Cyclotron waves on ITER operation around half-field

F.M. Poli

Princeton Plasma Physics Laboratory, Princeton, NJ, 08543, USA.

E-mail: fpoli@pppl.gov

D. Farina, L. Figini

Institute for Plasma Science and Technology, CNR, Milano, Italy

E. Poli

Max-Planck-Institute for Plasma Physics, 85748 Garching, Germany

Abstract. The ITER Research Plan envision operation around half of the nominal magnetic field (*i.e.* around $B = 2.65T$) as a path to baseline operation. This work discusses constraints on the optimal range of magnetic field, which is bounded in the lower limit by the presence of the third-harmonic Electron Cyclotron resonance at half field, and on the upper limit by the loss of core heating and current drive. It will be shown that increasing the magnetic field by only 3%, *i.e.* to 2.75T, eliminates the third harmonic parasitic absorption without compromising demonstration of access to H-mode, while operating at a magnetic field of 3.0T - previously proposed for optimal use of the Ion Cyclotron system - would impair the use of the Electron Cyclotron system for core-heating and current drive. Operation at 2.65T would still be possible if the polarization of the equatorial launcher is changed from X-mode to O-mode in the current flattop phase.

PACS numbers: 52.25,52.30,52.35,52.50,52.55,52.65

Submitted to: *Nuclear Fusion*

1. Introduction

ITER operation is divided into two periods, the first of which is plasma operation in both Hydrogen (H) and Helium (He) to avoid activation of the machine, followed by extensive Fusion Plasma Operation (FPO) with Deuterium (D) and Tritium (T) [1]. The non-activated period, or Pre-Fusion Plasma Operation (PFPO) is critical for machine and system qualification and is divided into three additional phases: First Plasma (FP), PFPO-1 and PFPO-2. The FP aims at demonstrating that the core tokamak components and systems can generate a plasma of at least 100kA for a duration of 100ms or longer. The second phase targets the first generation of an H-mode of up to 5 MA using the available 20 MW from the EC system in He and H at third field (1.8T) operation [2] and, pending on threshold limits, He at half field (2.65T). Demonstration of H-mode is crucial to validate the L to H-mode scaling, so that additional heating upgrades can occur prior to FPO operation. Only EC power is available in PFPO-1, thus requiring a scenario optimized for its performance. The third non-activated phase, PFPO-2, has the full contingency of the heating systems (an additional 20 MW IC and 33 MW NB), and ensures exploration of H-mode operation at half field with He plasmas. Note that access to H-mode in non-activated scenarios permits commissioning of the Edge Localized Modes mitigation schemes, the disruption mitigation system, assessing diverter heat loads and detachment, demonstrate controlled plasma termination and NTM control [1, 3].

The progress of the H-mode operation from the pure EC heated plasmas of PFPO-1 to the NB, IC and EC heated plasmas of PFPO-2, should utilise common scenarios in each phase as well as optimise the ratio of available power to the expected required H-mode threshold power. As the EC and IC powers are common to PFPO-2, scenarios should optimize both the EC and the IC performance to make use of all the available power. The assessment of the optimal operational space around half-field should consider all heating and current drive sources and provide compatible solutions that balance the available capabilities and provide a path from PFPO-1 to PFPO-2, as well as a path to FPO. Previous work on the assessment of PFPO-2 in plasmas with a mix of Helium and Hydrogen, considered operation at 2.65T and 7.5MA [3, 4], but did not discuss limitations due to parasitic absorption of the Electron Cyclotron waves on the third harmonic resonance off axis, which might indeed be dominant in these plasmas [5]. It will be shown here that, while operating around 2.75T would eliminate parasitic absorption, operation at 2.65T is still possible provided the wave polarization is changed from X-mode to O-mode after the transition from L-mode to H-mode. Since changing the polarization requires up to three seconds, during which the power would have a fraction of O-mode and X-mode coupling, a robust feedforward scheme is required to ensure that core heating and MHD stability control are maintained and that back transitions to L-mode are avoided. Operation with change of polarization has experimental evidence in present day devices, including stellarators, as discussed in the recent overview of W7-X [6].

		He	H
P_{NB} (MW)	E_{NB} (keV)	n_e [10^{19} m^{-3}]	n_e [10^{19} m^{-3}]
16.5	870	3	4.3
13.4	800	2.5	3.75
11.4	750	2.3	3.4
9.6	700	2	3.1
8.0	650	1.7	2.75
6.5	600	1.5	2.35
5.2	550	1.25	2
4.1	500	1	1.6

Table 1. Admissible density for injection of hydrogen beams in pure helium and pure hydrogen plasmas.

We notice that, in order to preserve the full capability of the EC system and not loose accessibility inside normalized radius of $\rho = 0.25$, the magnetic field should not exceed 2.85T [7]. These constrains reduce significantly the window for operation around half-field and might exclude plasmas with dominant Hydrogen fraction from this operation phase, since the Ion Cyclotron (ICRF) first pass absorption in hydrogen is low in this range of magnetic field [3, 8, 9]. While increasing the magnetic field up to 3.0T was suggested as a solution to the optimal use of ICRF in hydrogen plasmas [8], and is still the optimal solution for the commissioning and full assessment of the Ion Cyclotron system, the inability of using core ECH and ECCD would limit this option for operation with the full heating and current drive capabilities and for complete commissioning. All simulations discussed in this paper are assuming pure hydrogen plasma, for consistency in the discussion, when comparing plasmas at 2.65T and at 3.0T.
The paper is organized as follows: the assumptions of the models are discussed in Sec.2. An assessment of the parasitic absorption for magnetic field of 2.65T is discussed in Sec.3, the limitations of using the Electron Cyclotron system at magnetic field of 3.0T are discussed in Sec.5. Although the focus of this paper is not on scenario development, possible solutions for plasma scenarios at 2.65T are discussed in Sec.4, with a focus on the use of the Electron Cyclotron system. Obviously, an assessment of the deposition profiles and current drive could be done on fixed equilibrium and profiles and scanning the poloidal angle of the Equatorial Launcher, as it has already been done [7, 10]. However, the configuration of the Electron Cyclotron system affects the evolution of density and temperature profiles and the sawtooth period. For this reason, free-boundary time-dependent simulations that evolve both the magnetic equilibrium and the density and temperature profiles are used here, to provide a self-consistent assessment, yet within the limits of the models available in the time-dependent transport and equilibrium solver, in this case TRANSP [11, 12, 13]. The paper concludes with future directions and remaining, outstanding issues that need to be addressed by the integrated modeling community for a complete assessment of operation around half-field.

2. Modeling assumptions

All time-dependent simulations are run with the free-boundary equilibrium and transport solver TRANSP [11, 12, 13]. The simulation is initiated as a full-bore, limited plasma, with current of 100 kA, which is grown to full size and diverted at about 12-15s. The current flattop phase starts at 40s and ends at 330s, with L-H transition pre-programmed at the start of the flattop phase by Heating and Current Drive power and fueling. The threshold for the L-H transition is calculated based on the ITPA scaling [14]:

$$P_{L-H} = 2.84 m_H^{-1}\ B_0^{0.82} \bar{n_e}^{0.58} R\ a^{0.81} \tag{1}$$

The transition to H-mode occurs when the power across the separatrix exceeds the net power $P_{loss} - c_H P_{L-H}$, where the scaling factor c_H can be used to adjust the power threshold in those cases, like He plasmas, where the ITPA scaling would predict too high a threshold for transition compared to experimental evidence [15, 16, 17, 18]. Previous work focussing on ITER scenario assessment at half-field did assume a power threshold for Helium plasmas of 70% the value predicted by the ITPA scaling [3]. It is worth mentioning that recent experiments on ASDEX-U in Hydrogen plasmas with Helium doping up to 20% indicate that the H-mode power threshold stays at the levels of hydrogen plasmas [18].

At 2.65T and 7.5MA the power threshold for H-mode access is 40MW at densities of $n_e = 2.7\times10^{19}\mathrm{m}^{-3}$, which corresponds to 45% of the Greenwald density, and increases to 60MW for densities of $n_e = 4.7\times10^{19}\mathrm{m}^{-3}$, which corresponds to 75% of the Greenwald density. All simulations assume 73MW of external power available, with 33MW of NBI, 20MW of EC and 20MW of IC. Electron Cyclotron heating and current drive calculations are run with the beam tracing code TORBEAM [19, 20], Ion Cyclotron heating are done with TORIC5 [21] and Neutral Beam calculations with the MonteCarlo code NUBEAM [22]. Each Neutral Beam source can deliver up to 16.5 MW of power, with power and energy scaling according to $P_{MW} = 16.5\ (E/E_{Max})^{2.5}$, where E_{max}=1MeV for deuterium beams and 870keV for hydrogen beams. For hydrogen beams, Table 1 reports the values of admissible density to avoid shine through and the power load to the First Wall to exceed $2\mathrm{MW/m}^2$. According to Table 1, the beam source energy is selected in the time-dependent simulations to maintain some margins to account for uncertainties in the evolution of the plasma kinetic profiles and the plasma composition Z_{eff}, none of which is constant during the discharge. For a given density, the lowest beam energy is constrained by the threshold power for sustaining H-mode and the highest energy is constrained by the shine-through power. Impurity seeding with neon is considered in hydrogen plasmas to reduce the shine-thru power and allow the use of higher energy beams for sustainment of H-mode. Other impurities taken into account in the plasma composition are beryllium and tungsten.

Two identical ICRF antennas are part of the baseline H&CD configuration. The antennas operate at frequency in the range of 40-55 MHz to cover the magnetic field operational space. Each antenna is designed to deliver 20MW of power, however the baseline configuration distributes the power on the two antennas, independently operated, to reduce risks associated with failure of one of the antennas. A critical parameter for the IC heating is the maximum power coupled to the plasma as a function of the frequency. Since this is sensitive to the assumptions on the SOL density, in the absence of a self-consistent model for the propagation of the IC waves from the antenna to the core plasma, a parameterization would be needed for the correct accounting of losses outside the separatrix, which is not available at this time. Simulations assume therefore full coupling and absorption of the IC waves, a hypothesis that needs to be verified in future work.

Table 2 summarizes the settings used for the Electron Cyclotron simulations [7, 10, 23, 24]. The power is provided by 24 gyrotrons, connected to 24 transmission lines, operating at a frequency of 170 GHz and power of 1 MW each, of which 0.83 MW are delivered to the plasma on account of transmission losses from the gyrotron diamond window to the plasma boundary. There are two launchers: the Upper Launcher is located in four upper ports, each housing eight beam lines, arrayed in an upper and lower row of four waveguides each, dubbed Upper Steering (USM) and Lower Steering (LSM) mirror in the table. The Equatorial Launcher (EL) has three mirrors, dubbed as TOP (counter-current), MID and LOW (co-current) hosting each eight beams. Given the discrete nature of the beams, the poloidal and toroidal angles are inter-dependent and a variation of the poloidal steering angle does imply a (small) variation of the toroidal angle as well. For the purposes of scenario characterization, it is appropriate to treat each launching position using average values for the toroidal angle and leave the poloidal angle to steer. Thus, the angles indicated in Table 2 represent an averaging of the eight beams leaving the three steering mirrors of the EL, and an averaging of the four beams leaving the two steering mirrors of the ULs. In this frame, the toroidal angle is fixed and the poloidal angle is steerable. Using an EC-centered representation simplifies the algorithms for active feedback control, since only the poloidal angle needs to be adjusted. At the time of writing, further optimization of the design of the Equatorial Launcher was performed. The new configuration modifies the poloidal steering range of the bottom mirror from a downward steering to an upward steering, to minimize the opening in the blanket shielding module for neutron irradiation. The simulations reported in this paper do use the latest configuration, but the differences between the two geometries are discussed where appropriate.

2.1. Parametrization of the edge boundary

The time-dependent simulations use a parametrization for the values of density and temperature at the separatrix, based on the work by Kukushkin *et al* [25]. For the

sake of clarity and for completeness, some of the definitions are repeated herein, while maintaining the original labeling and providing reference to the equation number in the original work, where applicable. This scaling was derived for a carbon divertor environment and for a plasma with dominant helium composition, although a scan for the hydrogen fraction up to 90% was carried on, thus a systematic error is done here using this scaling in a tungsten environment and with hydrogen only. The goal here is to have a solution that evolves the transport equations and the equilibrium self-consistently within the limits of the models, by coupling the core and the edge while minimizing the number of prescribed transport parameters. We acknowledge here the limitations in this approach and defer to future work self-consistent simulations with core-edge integrated transport.

For a mixed helium-hydrogen plasma, the values at the separatrix for the thermal species and for beryllium are expressed by Eq.3-4 in [25]:

$$n_H = 0.0034 \left(\frac{\Gamma_H}{S_n \mu} \right)^{0.86} \tag{2}$$

$$n_{Be} = 1.1 \times 10^{-4} P_n^{0.66} \mu^{0.65} S_n^{0.33} \tag{3}$$

The electron density at the separatrix is calculated from the ion densities assuming quasi-neutrality, but excluding the contribution from carbon. TRANSP calculates the fluxes across the separatrix, Γ_H, based on the solution of particle balance, which are passed to the parametrization for the calculation of the temperature and density. The temperature at the separatrix is defined as (Equation 8 in Ref.[25]):

$$T_{i,sep} = 78 P_n n_i^{-1} \tag{4}$$

$$T_{e,sep} = 124 P_n^{0.56} n_e^{-0.4} \tag{5}$$

and is used as a boundary condition for the core thermal energy transport. The ratio of the beryllium to electron density at the separatrix is used as a representative value of the fraction of beryllium across the entire profile. This is an arbitrary assumption, but it is sufficient for the purposes of this work, where simulations attempt at evolving all parameters self-consistently within the limits of the models and of the assumptions. The normalized neutral pressure μ, the normalized pumping speed S_n and the normalized power across the SOL P_n are defined by Eq.(1) and (2) in Ref.[25]. Since these parameters are not used herein for feedback control, they are no further described here.

2.2. Parametrization of the pedestal

The turbulence transport model GLF23 [26, 27] is used to predict thermal energy transport for ions and electrons, momentum transport and electron particle transport. Impurity profiles are assumed to be the same shape as electron density profile, with the beryllium density fraction provided by Eq.2, tungsten density fraction fixed at 10^{-5} of the electron density and neon fraction up to 0.5% of the electron density. Beryllium is therefore the only impurity species that evolves in time. The main ion density profiles

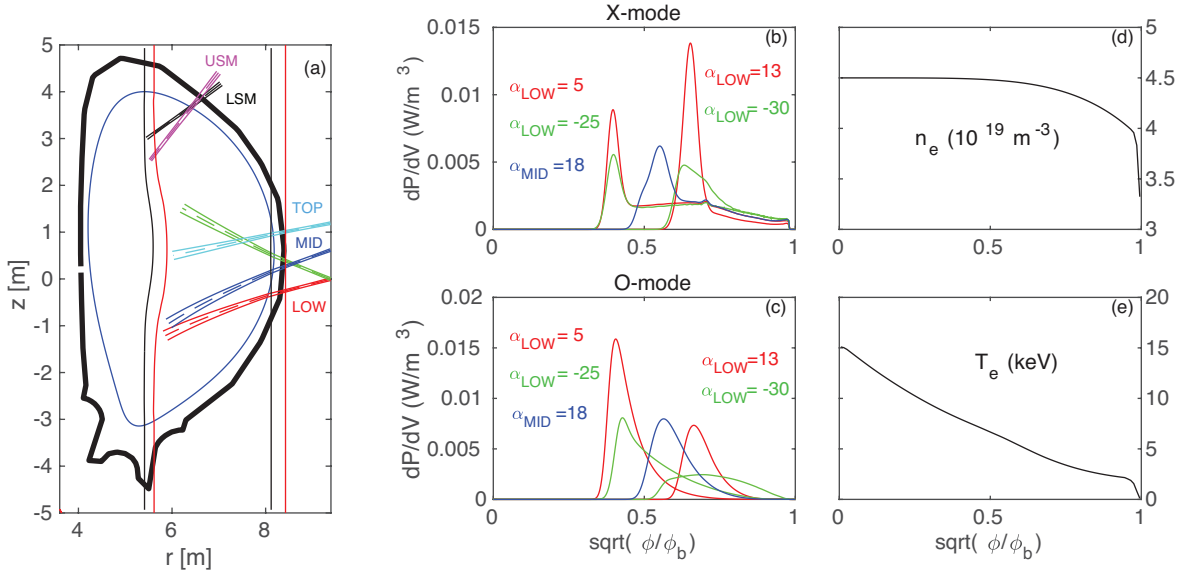

Figure 1. (a) beam trajectories from the Equatorial and Upper Launcher, in the current flattop of an ITER plasma with magnetic field of 2.65T, for poloidal angles of $\alpha_{USM} = 50.3°$, $\alpha_{LSM} = 35.7°$, $\alpha_{LOW} = 13°$ (red), $\alpha_{LOW} = -28°$ (green), $\alpha_{MID} = 18°$, $\alpha_{TOP} = 10°$. For the bottom mirror (LOW) ray trajectories are shown for both the old geometry (red) and for the latest geometry (green). The Electron Cyclotron cold 2nd and 3rd harmonic resonances location are shown for 2.65T (blue) and 2,75T (red). (b-c) Power density profile from the two co-current mirrors at 2.65T, with X-mode and O-mode polarization. For the LOW mirror two values of the poloidal angle are shown. (d) electron density profile used for the Electron Cyclotron beam calculations (e) electron temperature profiles.

Mirror	**R(m)**	**z(m)**	β	α **(min,max)**
TOP	9.394	1.192	-20	-10, +10
MID	9.394	0.62	25	5, 30
LOW	9.394	-0.004	25	-10, 25
(new)				-30, -10
USM	6.99871	4.41441	20	40, 65
LSM	7.05392	4.17821	20	30, 55

Table 2. Geometry used in TRANSP/TORBEAM for the Electron Cyclotron system. The toroidal angle indicated here is an average value and corresponds to assuming a single beam for each launching position, with focalized deposition at the resonance location. All angles are in the EC system frame.

are calculated from particle balance assuming quasi-neutrality.

In L-mode the boundary conditions for the electron and ion temperature and for the electron density are set by the values at the separatrix, calculated using the parametrization described above. In H-mode, the boundary conditions for the core transport are set by the pressure pedestal top width and height, which are calculated

from a neural network based upon calculations of peeling-ballooning stability limits provided by EPED1 [28], covering the ITER operational space at half-field and full-field [29]. For a general quantity y, which could be density or temperature, the profiles between the top of the pedestal and the separatrix are constructed using a hyperbolic tangent function:

$$y = y_0 \left\{ c_2(1 - r_2) \left[c_1 - \tanh\left(\frac{\psi - \psi_{ped}}{0.5\Delta_{ped}} \right) \right] + r_2 \right\} \tag{6}$$

where ψ is the normalized poloidal flux and ψ_{ped} is the normalized poloidal flux at the pedestal location. The pedestal width is therefore defined as $\Delta_{ped} = 1 - \psi_{ped}$. The top of the pedestal is defined as a point located $0.5\Delta_{ped}$ inside the pedestal, thus 1.5 times the pedestal width inside the separatrix. The parameter c_2 is defined as:

$$c_2 = \left(\frac{r_1 - r_2}{1 - r_2} \right) \frac{1}{2c_1} \tag{7}$$

with $r_2 = y_{sep}/y_0$, $r_1 = y_{ped}/y_0$ and $c_1 = \tanh(1)$. The pedestal density is assumed to be 0.61 $\bar{n}_e$, according to the NTCC pedestal model [30] and is an input to the EPED1-NN. Then, the electron temperature at the top of the pedestal is calculated from $p_{ped} \equiv 2n_{ped}kT_{ped}$ under the assumption that the pedestal structure in the electron and ion temperature are the same. Although this is not a situation encountered in the experiments, it is a common assumption in all models for the pedestal based on MHD stability calculations and on micro-turbulence that do not include kinetic effects.

3. Parasitic absorption of EC waves and operation around half-field

This section discusses limits on the operation around half-field and possible solutions for scenarios that maximize the use of all heating and current drive sources. The main constraint comes from the presence of the third harmonics layer inside the plasma at the magnetic field of 2.65T, which has direct implications on the minimum value of the magnetic field for operation that is free from parasitic absorption. The second constraint is on the radial location of the EC deposition, which has implications on the maximum value of the magnetic field at which operation is possible without losing the capabilities of the EC system. Both define an optimal configuration for the EC system in terms of polarization mode and range of poloidal steering angles for access to H-mode and for MHD control and on the IC system for maximization of the heating scheme. Either way, the optimal solution for the scenarios is one that maximizes the capabilities of both systems.

At 2.65T, which has been proposed as the value of magnetic field for operation in PFPO-2 [1], and with the nominal values of outer gap of 20cm, the third harmonics of the electron cyclotron frequency is inside the plasma, close to the plasma edge, as shown in Fig.1-(a). This causes parasitic absorption of the EC power at the plasma edge over the entire range of poloidal steering angle for the three mirrors in the Equatorial Launcher. The figure shows two trajectories for the bottom mirror, one (red) for the former poloidal

steering angle and one (green) for the most recent upgrade. We notice that the effect of the third harmonics parasitic absorption is present in both configurations.

This parasitic absorption limits the flexibility of the EC system for applications where controllable, localized deposition is required, like sawtooth pacing and core heating for impurity accumulation avoidance. It should be noticed that parasitic absorption at the third harmonics is independent of the plasma composition, thus it is observed both in hydrogen and helium plasmas and in deuterium and mix deuterium-tritium plasmas that might be developed as part of the path to $Q = 10$ during fusion operation. There are three ways to avoid parasitic absorption.

The first solution is to increase the outer plasma-wall gap by up to 10cm. In this case the value of q_{95} will be slightly higher than in plasmas with nominal value of the outboard plasma-wall gap. If the in-vessel coils are used for plasma vertical stabilization, the outboard plasma-wall gap can be increased up to 40 cm without modifying the inboard and upper plasma-wall gaps; this option is therefore well within the capabilities of the ITER control system. However, increasing the outer gap can reduce the coupling of the Ion Cyclotron waves to the plasma, an effect that cannot be assessed at this time in time-dependent simulations with TRANSP, since it requires a model for the antenna-plasma coupling and a self-consistent Scrape-Off-Layer model that evolves in time. This operational option is therefore not assessed herein.

The second solution is to operate at the second harmonics with O-mode polarization, where the effect of parasitic absorption is much lower due to the lower efficiency compared to X-mode. Both the O2 and X3 have lower optical depths than O1 and X2 by roughly a factor of T_e/mc^2 [31, 32]. The temperatures in H-mode result in optical depth for the O2 near unity (power being absorbed in the plasma core), while the X3 on the edge is sufficiently high resulting in the parasitic absorption on the plasma boundary. Note that the O3 optical depth is still thin with typical plasma parameters in H-mode, such that no parasitic absorption occurs for the O2 launch from the equatorial port. It should be noted that X2 from the upper launcher does not encounter the X3 parasitic absorption as the third harmonic resonance is well outside of the plasma due to the plasma curvature. Since the rays injected from the upper launcher do not intersect the third harmonics resonance layer, only the equatorial launcher would be operated in O-mode, while the Upper Launcher would still use X-mode polarization. Note that the heating profiles shown in Fig.1 have been calculated based upon a scenario that prescribes the shape of the electron density profile inside the pedestal, but predicts the pedestal width and height and the temperature profiles inside the separatrix. Because the deposition profile and the heating efficiency do change between O-mode and X-mode, the predicted profiles, including the current profile do respond to the heating and current drive efficiency, therefore a direct comparison of current drive efficiency for given injected power is not possible in exactly the same conditions. The deposition profiles are broader in O-mode for the new configuration for any given radial location and the current drive

efficiency is lower. While this does not cause significant differences in the scenarios, since most of the non-inductive current drive is provided by the Neutral Beams and the inductive Ohmic current is still dominant, it might affect control applications like sawtooth pacing. Possible solutions for operation at 2.65T include changing the polarization after the L-H transition, to maximize heating and current drive in L-mode, or operating the Equatorial Launcher in O-mode during the entire discharge. Both options are discussed in the following section.

The third solution is to increase the toroidal magnetic field to move the resonance layer outside the plasma. The power threshold for access to H-mode increases by 3% when the magnetic field is increased to 2.75T for a given line averaged density, according to the ITPA scaling [14]. To operate at 75% of the Greenwald density in hydrogen plasma, and accounting for partial absorption of the IC power, the full available power is needed to stay in H-mode, leaving no extra power available in case of failure of one of the systems.

4. Operation at 2.65T

As discussed in the previous section, operation at 2.65T might be possible by using the Equatorial Launcher at the second harmonics with O-mode wave polarization. Simulations of the current ramp-up phase have been run for hydrogen plasma, which are shown in Fig.2 (left column). The simulations assume same gas injection and same EC injected power and steering angles, but different wave polarization for the Equatorial Launcher bottom and mid mirror. The first case uses X-mode polarization (blue traces), the second case uses O-mode polarization (red traces). As shown in Fig.2-b, the case with O-mode polarization has lower absorbed power, about half of the total injected power, in the time window of $[20, 35]$s, then absorption gradually increases with increasing density, but it gets close to full absorption only in the flattop, while the case that uses X-mode wave polarization in L-mode achieves full absorption already at 20s. In both cases, the density needs to reach at least $1.5 \times 10^{19}\mathrm{m}^{-3}$ before at least 90% first pass absorption is obtained, with fluctuations around this value of density that depend on local values of the density profile. To emulate machine protection conditions, the simulation checks the value of the line averaged density value before turning-on the EC power. These simulations, which are predicting the density profile, indicate that operation at 2.65T and 7.5MA should use a combination of X-mode polarization in the ramp-up and in the initial portion of the flattop phase, then switch to O-mode wave polarization to minimize third harmonics parasitic absorption. In the flattop phase the absorption on O-mode is about 96% of the injected power, compared to 99% for X-mode, thus providing no significant loss of power for sustaining H-mode. The full discharge simulations aim at keeping the EC deposition at a normalized minor radius of 0.35-0.45, to avoid peaking of the safety factor profile at low density and high internal inductance, which might cause instabilities to develop in the plasma current ramp-up phase.

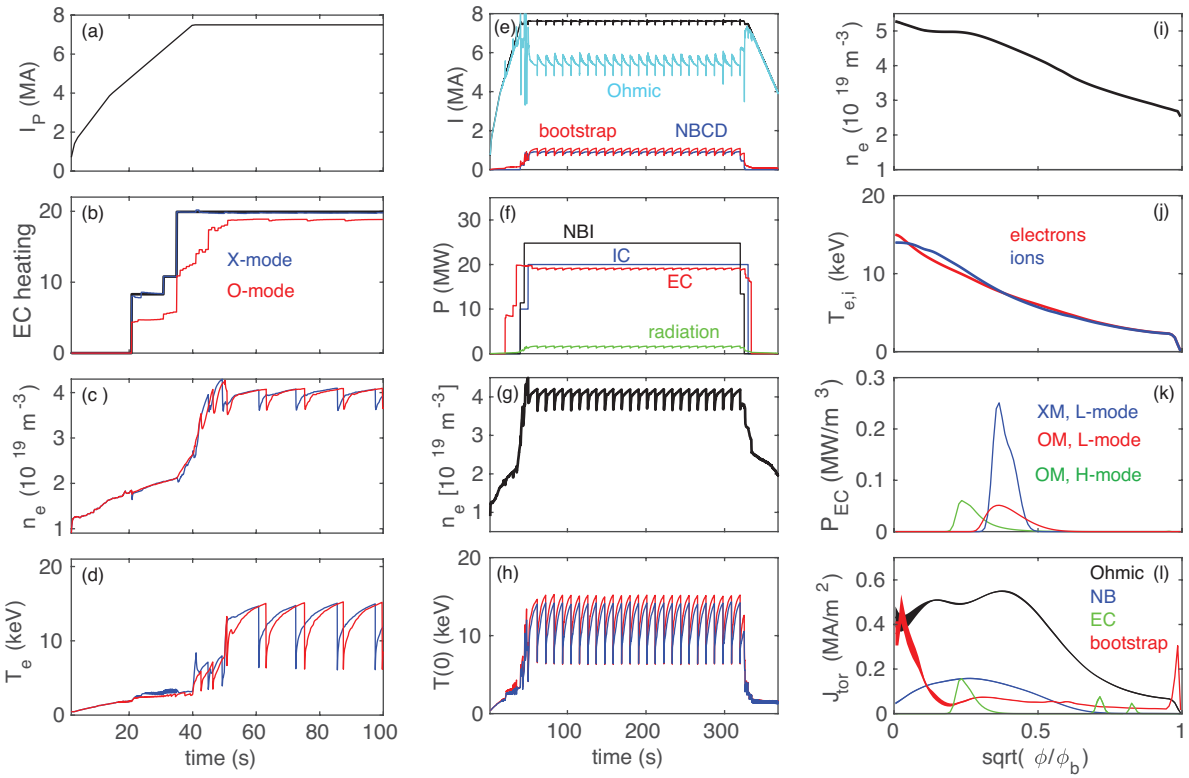

Figure 2. Left column: comparison between X-mode (blue) and O-mode (red) polarization in the current ramp-up phase. (a) plasma current (b) injected EC power (black) and absorbed power for X-mode polarization (blue) and for O-mode polarization (red) (c) line averaged electron density for the two simulations, with X-mode and O-mode polarization (d) central electron temperature. Central column: simulation of a hydrogen plasma at 2.65T, with transition from X-mode to O-mode polarization at 55s. (e) total current (thick) and contributions from Ohmic (black), neutral beam injection (blue) and bootstrap (red), (f) injected auxiliary power, Neutral Beams (black), Ion Cyclotron (blue), Electron Cyclotron (red) and radiation losses (green). (g) line averaged electron density (h) central value of electron and ion temperature. Right column: profiles in the flattop phase, average over 1s before each sawtooth crash (i) electron density (j) ion and electron temperature (k) comparison between the EC deposition in the flattop phase at 155s (green) and the deposition in L-mode, at 33s for X-mode (blue, same simulation) and O-mode (red, simulation shown in the left column) (l) profile of current contributions, average over 1s before each sawtooth crash.

Figure 2 (central column) shows a full discharge simulation of a hydrogen plasma for the same values of plasma current and magnetic field. The plasma enters H-mode between 40s and 50s, where uncertainties include density fueling and line averaged density evolution, as well as the timing of the auxiliary heating sources. The Neutral Beam power is 11.4MW on each beam and neon injection is used to stay below shine-thru limits. The wave polarization is switched from X-mode to O-mode at 55s, which is an arbitrary choice and based on the results shown in the left column. The wave polarization of the Upper Launcher is maintain at X-mode and a constant amount

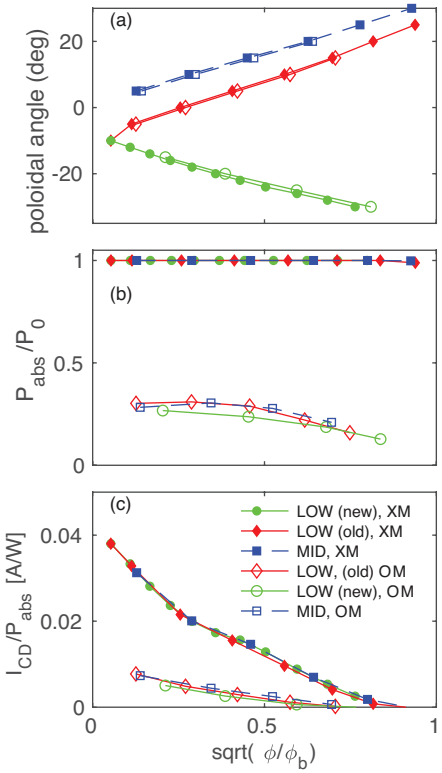

Figure 3. Scan of the poloidal steering angle for the bottom and mid mirror (both co-current injecting) in L-mode, calculated on the profiles at 33s from the simulations shown in Fig.2, left column.

of power is kept on either the upper and lower steering mirror, which are tracking respectively the $q = 1.5$ and $q = 2$ resonant surfaces. While third harmonics parasitic absorption is independent of the plasma composition, details of access to H-mode, density build-up and profile peaking, as well as edge density and temperature, depend on the background species and on the heating scheme. A full assessment of the scenario should evolve self-consistently all transport channels and include stability calculations and core-edge integrated transport for assessment of IC coupling, which is beyond the scope of this paper.

Profiles of selected plasma quantities are shown in the right column of Fig.2, as an average in the flattop phase, one second before each sawtooth crash. Profiles shown include the predicted electron density (a), the predicted electron and ion temperature (b), contributions to the toroidal current from Ohmic, bootstrap, Neutral Beam injection and Electron Cyclotron (d). Note that the phasing of the IC antenna is here chosen to provide only heating. Panel (c) compares the Electron Cyclotron heating profiles in H-mode (green) and in L-mode, at 33s (blue), the latter compared to the profile for O-mode polarization (red), extracted from the simulation shown in the left column.

Figure 3 shows the variation of absorbed power fraction and current drive efficiency with the poloidal steering angle for the two co-current mirrors and compares the old and

new configuration in the case of the bottom mirror. These calculations are done for given density and temperature profile in L-mode, extracted at 33s, from the time-dependent simulations shown in the left column of Fig.2. Open symbols refer to calculations with O-mode polarization and solid symbols refer to calculations with X-mode polarization. Differences in the current drive efficiency are small for the density and temperature profiles of these L-mode plasmas. However, it is noted that the absorbed power is lower in the case of the updated layout, with differences being larger for radial deposition around 0.35 and 0.45 of the minor radius, which is the optimal location for current profile tailoring in the current ramp-up.

Full discharge simulations for a hydrogen plasma at 2.75T and 7.8MA have also been undertaken. These simulations target the same electron density of the scenario at 2.65T and 7.5MA shown here, to ensure that the power threshold for H-mode access does not increase more than 3% compared to operation at 2.65T. Under these assumptions, the simulations look the same as those shown in Fig.2, except for using always X-mode polarization on the EC Equatorial Launcher, and do not add any valuable information to this discussion. They are therefore no further discussed here. These scenarios will be further developed in future work, with mix thermal ion species and full core-edge integration for assessment of the IC coupling.

5. EC operational limits on the magnetic field

Operating at magnetic field values of 3.0 and 3.3T during the non-active phase has been proposed as a solution to the lack of an efficient scheme for ion cyclotron heating in hydrogen plasmas at 2.65T [9, 3, 8]. The proposed heating scheme at increased magnetic field uses a small fraction of minority Helium-3 (about 1% of the electron density) at its fundamental resonance at 40MHz to achieve a single pass absorption of 80% and higher. However, at this magnetic field the Electron Cyclotron system would lose accessibility inside mid-radius, as shown by Farina *et al* [7]. The central column of Fig.4 shows a TRANSP simulation of a pure hydrogen plasma, with magnetic field of 3.0T and plasma current of 8.5MA, along the path of constant q_{95} to the ITER baseline operation. The output line averaged electron density in this simulation is $\bar{n}_e \simeq 4 \times 10^{19}\mathrm{m}^{-3}$, *i.e.* about 60% of the Greenwald density limit ($\bar{n}_e \simeq 6.8 \times 10^{19}\mathrm{m}^{-3}$ at this current). At this density and in pure hydrogen plasma, the minimum beam energy to avoid shine through is 800keV, which corresponds to 13.4MW on each beamline [33]. At this density the power threshold for H-mode access is 43MW. Assuming 100% IC coupling and absorption, 20MW of EC power and accounting for beam shine through losses, the total power across the separatrix is only 10% above the power threshold for the L-H transition when using two sources at 750keV and 11.4MW each, and 17% above the power threshold when using 11.4MW on one beamline and 16.5MW on the second beamline. The former case is compatible with shine through limits even in pure hydrogen plasmas, the latter needs either impurity injection or helium doping up to 20% (or both) to decrease the shine-through limit at this density. The case shown in

the figure uses one source at 750keV at low density at the end of the current ramp-up phase and one source at full power about three seconds later, with neon injection in the flattop phase.

The Equatorial launcher is used with poloidal angle of 6 degrees on the intermediate mirror and with -10 degrees on the lower mirror, to distribute the deposition while maintaining core heating at the innermost radial location that can be reached. Based upon the equilibrium and profiles predicted at 150s, a scan of the poloidal angle has been done on all three mirrors, which is shown in the left column of Fig.4. The innermost radial location that the two co-current injection mirrors can reach is about 0.45, while it is about 0.30 for the counter-injecting mirror. These are also the locations where the current drive efficiency is highest. We notice that the innermost radial location that the lower mirror can reach is slightly more off-axis in the case of the updated poloidal steering range, but differences in the current drive efficiency and deposition profile are very small.

This scenario at 3.0T is still feasible for demonstration of access and sustainment of H-mode in pure hydrogen plasmas, with the full available power, provided the density does not exceed 60% of the Greenwald density limit. However, losing the accessibility of the EC system inside mid-radius limits the flexibility of the system for sawtooth pacing, current profile tailoring and core heating for impurity influx control. If access to reverse shear plasmas is needed for demonstration of steady state operation, then the top mirror cannot be used for counter-current drive. Another limitation with operation at this magnetic field is the feasibility of a controlled ramp-down phase. When the plasma cross-section is reduced in size and the plasma is guided downward to reduce the internal inductance and avoid the plasma from becoming vertically unstable, the EC system is the only one that can follow the plasma centroid. These scenarios at 3.0T need to be assessed for heat loads to the plasma wall during teh termination phase.

6. Conclusions

Operation around half-field is part of the ITER Research Plan as a path to full field operation. Plasma scenarios will be used to commission the heating and current drive systems, demonstrate access to H-mode, demonstrate ELM control and NTM control. They will also serve to commission the plasma control system for the termination phase, including managing the exit from H-mode in the presence of alphas at lower magnetic field and lower poloidal beta. Access to H-mode in non-activated scenarios permits commissioning of the Edge Localized Modes mitigation schemes, the disruption mitigation system, assessing diverter heat loads and detachment, demonstrate controlled plasma termination and NTM control [1]. The progress of the H-mode operation from the pure EC heated plasmas of PFPO-1 to the NB, IC and EC heated plasmas of PFPO-2, should utilise common scenarios in each phase as well as optimise the ratio of available power to the expected required H-mode threshold power. As the EC and IC powers are common to both PFPO-1 and PFPO-2, scenarios should optimize both

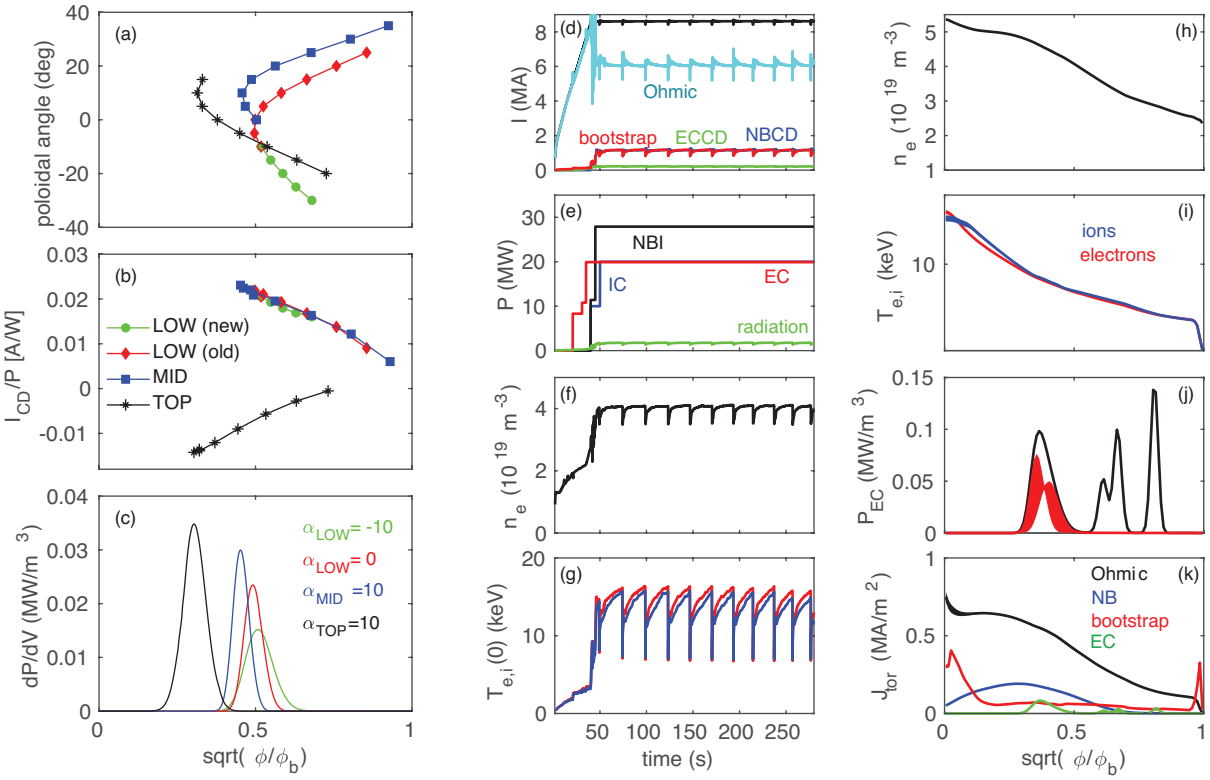

Figure 4. Left column: results from a scan of the poloidal steering angle, for profiles extracted at 155s from the simulation shown in the central column. (a) radial location of the peak current deposition, poloidal angle vs normalized radius (b) current drive efficiency (c) profiles of absorbed power and current drive for selected poloidal angle. Central column: simulation of a hydrogen plasma at 3.0T. (d) total current (thick) and contributions from Ohmic (black), neutral beam injection (blue) and bootstrap (red), (e) injected auxiliary power, Neutral Beams (black), Ion Cyclotron (blue), Electron Cyclotron (red) and radiation losses (green). (f) line averaged electron density (g) central value of electron and ion temperature. Right column: profiles in the flattop phase, average over 1s before each sawtooth crash (h) electron density (l) ion and electron temperature (j) average total EC deposition (black) and variation for the Equatorial Launcher (k) profile of current contributions, average over 1s before each sawtooth crash.

the EC and the IC performance. However, at 2.65T and 7.5MA, which corresponds to exactly half value of the nominal ITER magnetic field, the Electron Cyclotron waves are affected by parasitic absorption at the third harmonics. This effect is present for all mirrors in the Equatorial Launcher and is independent of the plasma composition. The amplitude of the parasitic absorption depends on local values of the electron density and temperature, which modify the optical depth of the plasma. The geometry of the EC Equatorial Launcher has recently been updated to simplify the engineering design and reduce the opening in the blanket, to minimize neutron irradiation. The new poloidal steering angle range of the lower mirror entirely falls within the vertical region affected by the third harmonics parasitic absorption, with an effect that is larger than in the case

of the previous layout. This does not compromise the use of the EC system, but requires adjustments to the operational space to fully exploit the capabilities of the system.

Simulations have been run with TRANSP, where the density and temperature at the separatrix are calculated from a parametrization of SOLPS calculations [25] and are evolved dynamically, coupled with the core transport fluxes. These simulations assess the absorption in L-mode and in H-mode and propose solutions for operation around half-field, that minimize the effect of the third harmonics absorption. Operation at 2.65T is still possible provided the wave polarization is changed from X-mode to O-mode shortly after the beginning of the plasma current flattop phase. However, switching the polarization takes about three seconds, during which the polarization is a mix of O-mode and X-mode. Also, the decreased power absorption in O-mode might trigger back-transitions to L-mode, thus this phase of the discharge needs to be controlled. Operation at 2.75T should be therefore preferred, because X-mode polarization can be maintained during the entire discharge, thus simplifying the number of combined operation of the Plasma Control System, since first pass absorption should be monitored as the density evolves. The small increase of the magnetic field, only 3%, has a minor effect on the power threshold for H-mode access and sustainment, if the plasma operates at a density of about 60% of the Greenwald limit. Helium doping might be needed to decrease shine-through limits and operate with both neutral beams at the maximum energy and power, to sustain H-mode with power at least 20% above the L-H transition power threshold, for safety margins to balance reduced IC coupling and/or absorption and dynamical variations of the EC power, as a consequence of switching the power between the Equatorial and Upper Launcher for combined control of Neoclassical Tearing Modes and of the sawtooth period.

Operation at higher magnetic field has limitations due to the fact that the higher the field the more the innermost reachable location moves to larger radial locations. Operating at 3.0T has been proposed as a solution to ensure first pass absorption of the IC waves, with a small fraction of Helium3 minority heating [8]. At these values of the magnetic field the EC system loses access inside mid-radius, thus limiting applications like current profile tailoring for control of the sawtooth period. Impurity influx needs to be assessed with self-consistent simulations to compare the effectiveness of Ion Cyclotron vs Electron Cyclotron heating for core electron heating for control of impurity influx.

While the conclusions on the third harmonics parasitic absorption and solutions to avoid it are valid, since independent of the transport models used, a full assessment of the scenarios for optimization of synergistic use of all heating and current drive systems should include self-consistent transport in all channels, energy, momentum and particle, a coupled core-edge transport model, including modeling of the losses of IC waves in the SOL in dynamical conditions, as well as modeling of MHD and Energetic Particle stability and their effects on the redistribution of fast ions.

The authors thank Mark Henderson for encouraging this work and for valuable discussion on the optics of the Electron Cyclotron system. This work is supported in part by the U.S. Department of Energy, Office of Science, Office of Fusion Energy Sciences under contract number DE-AC02-09CH11466. The views and opinions expressed herein do not necessarily reflect those of the ITER Organization.

[1] ITER Organization. Iter research plan within the staged approach (level iii ? provisional version), report itr-18-003, September 2018.

[2] M. Schneider, A.R. Polevoi, S.H. Kim, A. Loarte, S.D. Pinches, J-F. Artaud, E. Militello-ASP, B. Beaumont, R. Bilato, D. Boilson, D.J. Campbell, P. Dumortier, D. Farina, L. Figini, Y. Gribov, M. Henderson, R.R. Khayrutdinov, A.A. Kavin, F. Köchl, T. Kurki-Suonio, A. Kuyanov, P. Lamalle, E. Lerche, V.E. Lukash, A. Messiaen, V. Parail, K. Särkimäki, A. Snicker, and D. Van Eester and. Modelling one-third field operation in the ITER pre-fusion power operation phase. Nuclear Fusion, 59(12):126014, sep 2019.

[3] S.H. Kim, F.M. Poli, F. Koechl, E. Militello-Asp, A.R. Polevoi, R. Budny, T.A. Casper, A. Loarte, T.C. Luce, Y.-S. Na, M. Romanelli, M. Schneider, J.A. Snipes, P.C. de Vries, and The ITPA Topical Group on Integrated Operation Scenarios. Nuclear Fusion, 53(12):123026, 2013.

[4] A.R. Polevoi, D.J. Campbell, V.A. Chuyanov, W. Houlberg, A.A. Ivanov, A.S. Kukushkin, P. Lamalle, A. Loarte, V.S. Mukhovatov, and T. Oikawa. Nuclear Fusion, 57(8):086021, 2017.

[5] Poli F M et al. Electron cyclotron power management in iter, the path from the commissioning phase to demonstration discharges. In Preprint: 2016 IAEA Fusion Energy Conference, 2016.

[6] R.C. Wolf, A. Ali, A. Alonso, J. Baldzuhn, C. Beidler, M. Beurskens, C. Biedermann, H.-S. Bosch, S. Bozhenkov, R. Brakel, A. Dinklage, Y. Feng, G. Fuchert, J. Geiger, O. Grulke, P. Helander, M. Hirsch, U. Höfel, M. Jakubowski, J. Knauer, G. Kocsis, R. König, P. Kornejew, A. Krämer-Flecken, M. Krychowiak, M. Landreman, A. Langenberg, H.P. Laqua, S. Lazerson, H. Maaßberg, S. Marsen, M. Marushchenko, D. Moseev, H. Niemann, N. Pablant, E. Pasch, K. Rahbarnia, G. Schlisio, T. Stange, T. Sunn Pedersen, J. Svensson, T. Szepesi, H. Trimino Mora, Y. Turkin, T. Wauters, G. Weir, U. Wenzel, T. Windisch, G. Wurden, D. Zhang, I. Abramovic, S. Äkäslompolo, P. Aleynikov, K. Aleynikova, R. Alzbutas, G. Anda, T. Andreeva, E. Ascasibar, J. Assmann, S.-G. Baek, M. Banduch, T. Barbui, M. Barlak, K. Baumann, W. Behr, A. Benndorf, O. Bertuch, W. Biel, D. Birus, B. Blackwell, E. Blanco, M. Blatzheim, T. Bluhm, D. Böckenhoff, P. Bolgert, M. Borchardt, V. Borsuk, J. Boscary, L.-G. Böttger, H. Brand, Ch. Brandt, T. Bräuer, H. Braune, S. Brezinsek, K.-J. Brunner, B. Brünner, R. Burhenn, B. Buttenschön, V. Bykov, I. Calvo, B. Cannas, A. Cappa, A. Carls, L. Carraro, B. Carvalho, F. Castejon, A. Charl, F. Chernyshev, M. Cianciosa, R. Citarella, Ł. Ciupiński, G. Claps, M. Cole, M.J. Cole, F. Cordella, G. Cseh, A. Czarnecka, A. Czermak, K. Czerski, M. Czerwinski, G. Czymek, A. da Molin, A. da Silva, G. Dammertz, A. de la Pena, S. Degenkolbe, P. Denner, D.P. Dhard, M. Dostal, M. Drevlak, P. Drewelow, Ph. Drews, A. Dudek, G. Dundulis, F. Durodie, P. van Eeten, F. Effenberg, G. Ehrke, M. Endler, D. Ennis, E. Erckmann, H. Esteban, T. Estrada, N. Fahrenkamp, J.-H. Feist, J. Fellinger, H. Fernandes, W.H. Fietz, W. Figacz, J. Fontdecaba, O. Ford, T. Fornal, H. Frerichs, A. Freund, M. Führer, T. Funaba, A. Galkowski, G. Gantenbein, Y. Gao, J. García Regaña, M. Garcia-Munoz, D. Gates, G. Gawlik, B. Geiger, V. Giannella, N. Gierse, A. Gogoleva, B. Goncalves, A. Goriaev, D. Gradic, M. Grahl, J. Green, A. Grosman, H. Grote, M. Gruca, C. Guerard, L. Haiduk, X. Han, F. Harberts, J.H. Harris, H.-J. Hartfuß, D. Hartmann, D. Hathiramani, B. Hein, B. Heinemann, P. Heitzenroeder, S. Henneberg, C. Hennig, J. Hernandez Sanchez, C. Hidalgo, H. Hölbe, K.P. Hollfeld, A. Hölting, D. Höschen, M. Houry, J. Howard, X. Huang, M. Huber, V. Huber, H. Hunger, K. Ida, T. Ilkei, S. Illy, B. Israeli, A. Ivanov, S. Jablonski, J. Jagielski, J. Jelonnek, H. Jenzsch, P. Junghans, J. Kacmarczyk, T. Kaliatka, J.-P. Kallmeyer, U. Kamionka, R. Karalevicius, H. Kasahara, W. Kasparek, N. Kenmochi, M. Keunecke, A. Khilchenko, D. Kinna, R. Kleiber, T. Klinger, M. Knaup, Th. Kobarg, F. Köchl, Y. Kolesnichenko, A. Könies, M. Köppen, J. Koshurinov, R. Koslowski, F. Köster, R. Koziol, M. Krämer, R. Krampitz, P. Kraszewsk, N. Krawczyk, T. Kremeyer, Th. Krings, J. Krom, G. Krzesinski, I. Ksiazek, M. Kubkowska, G. Kühner, T. Kurki-Suonio, S. Kwak, R. Lang, S. Langish, H. Laqua, R. Laube, C. Lechte, M. Lennartz, W. Leonhardt, L. Lewerentz, Y. Liang, Ch. Linsmeier, S. Liu, J.-F. Lobsien, D. Loesser, J. Loizu Cisquella, J. Lore, A. Lorenz, M. Losert, L. Lubyako, A. Lücke, A. Lumsdaine, V. Lutsenko, J. Majano-Brown, O. Marchuk, M. Mardenfeld, P. Marek,

S. Massidda, S. Masuzaki, D. Maurer, K. McCarthy, P. McNeely, A. Meier, D. Mellein, B. Mendelevitch, Ph. Mertens, D. Mikkelsen, O. Mishchenko, B. Missal, J. Mittelstaedt, T. Mizuuchi, A. Mollen, V. Moncada, T. Mönnich, T. Morizaki, R. Munk, S. Murakami, F. Musielok, G. Náfrádi, M. Nagel, D. Naujoks, H. Neilson, O. Neubauer, U. Neuner, T. Ngo, R. Nocentini, C. Nührenberg, J. Nührenberg, S. Obermayer, G. Offermanns, K. Ogawa, J. Ongena, J.W. Oosterbeek, G. Orozco, M. Otte, L. Pacios Rodriguez, W. Pan, N. Panadero, N. Panadero Alvarez, A. Panin, D. Papenfuß, S. Paqay, A. Pavone, E. Pawelec, G. Pelka, X. Peng, V. Perseo, B. Peterson, A. Pieper, D. Pilopp, S. Pingel, F. Pisano, B. Plaum, G. Plunk, M. Povilaitis, J. Preinhaelter, J. Proll, M.-E. Puiatti, A. Puig Sitjes, F. Purps, M. Rack, S. Récsei, A. Reiman, D. Reiter, F. Remppel, S. Renard, R. Riedl, J. Riemann, S. Rimkevicius, K. Rißе, A. Rodatos, H. Röhlinger, M. Romé, P. Rong, H.-J. Roscher, B. Roth, L. Rudischhauser, K. Rummel, T. Rummel, A. Runov, N. Rust, L. Ryc, S. Ryosuke, R. Sakamoto, A. Samartsev, M. Sanchez, F. Sano, S. Satake, G. Satheeswaran, J. Schacht, F. Schauer, T. Scherer, A. Schlaich, K.-H. Schlüter, J. Schmitt, H. Schmitz, O. Schmitz, S. Schmuck, M. Schneider, W. Schneider, M. Scholz, P. Scholz, R. Schrittwieser, M. Schröder, T. Schröder, R. Schroeder, H. Schumacher, B. Schweer, B. Shanahan, I.V. Shikhovtsev, M. Sibilia, P. Sinha, S. Sipliä, J. Skodzik, C. Slaby, H. Smith, W. Spiess, D.A. Spong, A. Spring, R. Stadler, B. Standley, L. Stephey, M. Stoneking, U. Stridde, Z. Sulek, Y. Suzuki, V. Szabó, T. Szabolics, Z. Szökefalvi-Nagy, N. Tamura, A. Terra, J. Terry, J. Thomas, H. Thomsen, M. Thumm, C.P. von Thun, D. Timmermann, P. Titus, K. Toi, J.M. Travere, P. Traverso, J. Tretter, H. Tsuchiya, T. Tsujimura, S. Tulipán, M. Turnyanskiy, B. Unterberg, J. Urban, E. Urbonavicius, I. Vakulchyk, S. Valet, B. van Millingen, L. Vela, J.-L. Velasco, M. Vergote, M. Vervier, N. Vianello, H. Viebke, R. Vilbrandt, A. Vorkörper, S. Wadle, F. Wagner, E. Wang, N. Wang, F. Warmer, L. Wegener, J. Weggen, Y. Wei, J. Wendorf, A. Werner, B. Wiegel, F. Wilde, E. Winkler, V. Winters, S. Wolf, J. Wolowski, A. Wright, P. Xanthopoulos, H. Yamada, I. Yamada, R. Yasuhara, M. Yokoyama, J. Zajac, M. Zarnstorff, A. Zeitler, H. Zhang, J. Zhu, M. Zilker, A. Zimbal, A. Zocco, S. Zoletnik, and M. Zuin. Major results from the first plasma campaign of the wendelstein 7-x stellarator. Nuclear Fusion, 57(10):102020, jul 2017.

[7] D. Farina, M. Henderson, L. Figini, G. Ramponi, and G. Saibene. Potential of the ITER electron cyclotron equatorial launcher for heating and current drive at nominal and reduced fields. Nuclear Fusion, 52(3):033005, feb 2012.

[8] M. Schneider at al. EPJ, RF topical conference, 2017.

[9] S.H. Kim et al. In Proceedings of 41st EPS Conf. on Plasma Physics, 2014.

[10] D. Farina, M. Henderson, L. Figini, and G. Saibene. Optimization of the iter electron cyclotron equatorial launcher for improved heating and current drive functional capabilities. Physics of Plasmas, 21(6):061504, 2014.

[11] Hawryluk R. An Empirical Approach To Tokamak Transport. In Physics of Plasmas Close to Thermonuclear Conditions Proceedings of the Course Held in Varenna, Italy, 27 August-8 September 1979, pages 19–46. Elsevier Ltd., 1981.

[12] Joshua Breslau, Marina Gorelenkova, Alexei Pankin, Gopan Perumpilly, Francesca Poli, and Jai Sachdev. Transp. [Computer Software] urlhttps://doi.org/10.11578/dc.20180627.4, jun 2018.

[13] R. Andre. TRANSP/PTRANSP Isolver free boundary equilibrium solver. In Bull. Am. Phys. Soc., 2012.

[14] Martin YR *et al.* Journal of Physics: Conf. Series, 123:012033, 2008.

[15] M Bessenrodt-Weberpals, F Wagner, O Gehre, L Giannone, J.V Hofmann, A Kallenbach, K McCormick, V Mertens, H.D Murmann, F Ryter, B.D Scott, G Siller, F.X Soldner, A Stabler, K.-H Steuer, U Stroth, N Tsois, H Verbeek, and H Zoohm. The isotope effect in ASDEX. Nuclear Fusion, 33(8):1205–1238, aug 1993.

[16] A. Kallenbach for the ASDEX Upgrade Team and the EUROfusion MST1 Team. Overview of ASDEX upgrade results. Nuclear Fusion, 57(10):102015, jun 2017.

[17] C.E. Kessel, S.M. Wolfe, M.L. Reinke, J.W. Hughes, Y. Lin, S.J. Wukitch, S.G. Baek, P.T. Bonoli,

M. Chilenski, and A. Diallo. Helium experiments on alcator c-mod in support of ITER early operations. Nuclear Fusion, 58(5):056007, mar 2018.

[18] U. Plank, T. Pütterich, C. Angioni, M. Cavedon, G. D. Conway, R. Fischer, T. Happel, A. Kappatou, R. M. McDermott, P. A. Schneider, G. Tardini, M. Weiland, and ASDEX Upgrade team. H-mode power threshold studies in mixed ion species plasmas at ASDEX upgrade. Nuclear Fusion, 60(7):074001, jun 2020.

[19] Poli E *et al.* Comput. Phys. Commun., 136:90, 2001.

[20] E. Poli, A. Bock, M. Lochbrunner, O. Maj, M. Reich, A. Snicker, A. Stegmeir, F. Volpe, N. Bertelli, R. Bilato, G.D. Conway, D. Farina, F. Felici, L. Figini, R. Fischer, C. Galperti, T. Happel, Y.R. Lin-Liu, N.B. Marushchenko, U. Mszanowski, F.M. Poli, J. Stober, E. Westerhof, R. Zille, A.G. Peeters, and G.V. Pereverzev. Torbeam 2.0, a paraxial beam tracing code for electron-cyclotron beams in fusion plasmas for extended physics applications. Computer Physics Communications, 225:36–46, 2018.

[21] Marco Brambilla. Plasma Physics and Controlled Fusion, 44(11):2423, 2002.

[22] RJ *et al* Goldston. J. Comput. Phys., 43:61, 1981.

[23] M.A. Henderson, G. Saibene, and G. Darbos. Phys. Plasmas, 22:021808, 2015.

[24] M.A. Henderson, R. Chavan, and R. Bertizolo *et al.* Fusion Sci. Techn., 53:139, 2008.

[25] A.S. Kukushkin, H.D. Pacher, V. Kotov, G.W. Pacher, R.A. Pitts, and D. Reiter. ITER divertor performance in the low-activation phase. Nuclear Fusion, 53(12):123025, nov 2013.

[26] Waltz R.E. *et al.* Phys. Plasmas, 4:2481, 1997.

[27] Kinsey J.E. *et al.* Fusion Sci. and Tech., 44:763, 2003.

[28] Snyder P.B. *et al.* Nucl. Fusion, 51:103016, 2011.

[29] O. Meneghini, S.P. Smith, P.B. Snyder, G.M. Staebler, J. Candy, E. Belli, L. Lao, M. Kostuk, T. Luce, T. Luda, J.M. Park, and F. Poli. Nuclear Fusion, 57(8):086034, 2017.

[30] T. Onjun, G. Bateman, A. H. Kritz, and G. Hammett. Models for the pedestal temperature at the edge of h-mode tokamak plasmas. Physics of Plasmas, 9(12):5018–5030, 2002.

[31] R. Prater. Heating and current drive by electron cyclotron waves. Physics of Plasmas, 11(5):2349–2376, 2004.

[32] M. Bornatici, R. Cano, O. De Barbieri, and F. Engelmann. Electron cyclotron emission and absorption in fusion plasmas. Nuclear Fusion, 23(9):1153–1257, sep 1983.

[33] M J Singh, D Boilson, A R Polevoi, Toshihiro Oikawa, and Raphael Mitteau. Heating neutral beams for ITER: negative ion sources to tune fusion plasmas. New Journal of Physics, 19(5):055004, may 2017.